Supermassive Stars Match the Spectral Signatures of JWST's Little Red Dots

Devesh Nandal[1] and Abraham Loeb[2]

[1]*Department of Astronomy, University of Virginia, 530 McCormick Rd, Charlottesville, VA 22904, USA*
[2]*Center for Astrophysics, Harvard and Smithsonian, 60 Garden St, Cambridge, MA 02138, USA*

ABSTRACT

The James Webb Space Telescope (JWST) has unveiled a population of enigmatic, compact sources at high redshift known as "Little Red Dots" (LRDs), whose physical nature remains a subject of intense debate. Concurrently, the rapid assembly of the first supermassive black holes (SMBHs) requires the formation of heavy seeds, for which supermassive stars (SMSs) are leading theoretical progenitors. In this work, we perform the first quantitative test of the hypothesis that LRDs are the direct observational manifestation of these primordial SMSs. We present a novel, first-principles pipeline generating synthetic spectra for a non-rotating, metal-free $10^6 \, M_\odot$ SMS. We establish that its luminosity ($L_\lambda \approx 1.7 \times 10^{44} \, \mathrm{erg \, s^{-1} \, \mu m^{-1}}$ at $4050 \, \text{Å}$) provides a decisive constraint, matching prominent LRDs. Our model self-consistently reproduces their defining spectral features: the extreme, V-shaped Balmer break is an intrinsic photospheric effect, while the complex line phenomenology, strong $H\beta$ in emission with other Balmer lines in absorption arises from non-LTE effects in a single stellar atmosphere. Applying physically motivated broadening, our spectrum provides an excellent quantitative match to LRDs at both high ($z = 7.76$) and low ($z = 3.55$) redshift. Our model provides a simple, self-consistent physical picture for LRDs, offering a compelling alternative to multi-component obscured AGN scenarios and suggesting we may be directly witnessing the final, luminous moments of an SMBH progenitor before its ultimate collapse.

Keywords: Massive stars (732) — Stellar evolutionary models (2046) — Supermassive black holes (1663) — Early universe (435) — Stellar accretion (1578)

1. INTRODUCTION

The discovery of quasars with black hole masses $\gtrsim 10^9 \, M_\odot$ at $z \gtrsim 7$ demands seeds of at least 10^{4}–$^5 \, M_\odot$ that grow efficiently within the first $\sim 0.6 \, \mathrm{Gyr}$ of cosmic history (X. Fan et al. 2006; K. Inayoshi et al. 2020; M. Volonteri et al. 2021). A physically motivated pathway invokes *supermassive stars* (SMSs) that form in pristine, atomic cooling haloes where the suppression of H_2 cooling prevents fragmentation, allowing for inflows of $\dot{M} \sim 0.1$–$10 \, M_\odot \, \mathrm{yr^{-1}}$ (A. Loeb & F. A. Rasio 1994; V. Bromm & A. Loeb 2003; M. C. Begelman 2012; T. Hosokawa et al. 2012; L. Haemmerlé et al. 2018). Stellar structure calculations show that such objects inflate to $\sim 10^4 \, R_\odot$, radiate near the Eddington limit, and collapse by general relativistic instability once the core reaches a few $10^5 \, M_\odot$ (T. W. Baumgarte & S. L. Shapiro 1999; T. E. Woods et al. 2017; L. Haemmerlé 2021). A complementary formation channel operates

during major gas rich mergers, where global torques drive extreme inflow rates of $\sim 10^3$–$10^4 \, M_\odot \, \mathrm{yr^{-1}}$ into a sub-parsec disc that fragments minimally and feeds a transient SMS which collapses almost directly into a 10^6–$10^7 \, M_\odot$ black hole (L. Mayer et al. 2010a, 2015; L. Zwick et al. 2023). These routes provide seed masses and duty cycles consistent with the luminosity function of high redshift quasars (F. Pacucci & A. Loeb 2022).

A decisive observational signature of SMS–dominated epochs would be stellar photospheres that exhibit strong Balmer discontinuities, broad Balmer emission, and negligible metal lines because envelopes remain metal poor and radiation pressure supported (D. R. G. Schleicher et al. 2019; F. Martins et al. 2020; P. Natarajan 2021). Such spectral behaviour naturally arises when the $n = 2$ hydrogen population is driven out of local thermodynamic equilibrium (NLTE) by the intense stellar continuum, boosting the Balmer continuum opacity and causing the photospheric break to deepen while a low collisional destruction probability forces H I $H\beta$ into emission (L. H. Auer & D. Mihalas 1969). These unique features

Email: deveshnandal@yahoo.com

are challenging to replicate with standard stellar populations or typical AGN models, making them a distinct fingerprint of SMS physics.

JWST observations have recently revealed a compact population dubbed "Little Red Dots" (LRDs), characterised by radii $\lesssim 100\,\mathrm{pc}$, luminosities $\gtrsim 10^{11}\,L_\odot$, Balmer breaks of $\gtrsim 1.5\,\mathrm{dex}$, broad H$\beta$ or Hα with FWHM $\sim 10^3$–$10^4\,\mathrm{km\,s^{-1}}$, and an almost complete absence of metal features or X-ray counterparts (I. Labbé et al. 2023; V. Kokorev et al. 2023; J. F. W. Baggen et al. 2024; J. Matthee et al. 2024; Z. Zhang et al. 2025). Photometric and kinematic analyses suggest stellar masses of 10^{10}–$10^{11}\,M_\odot$ packed within $\lesssim 0.3\,\mathrm{kpc}$, yielding stellar velocity dispersions comparable to their Balmer line widths (J. F. W. Baggen et al. 2024; M. Killi et al. 2024). Conventional active galactic nucleus templates struggle to match the simultaneous presence of a deep Balmer break and X-ray silence (H. Übler et al. 2024), while pure starburst models fail to generate the observed broad lines without invoking implausibly young but massive clusters.

SMS photospheres resolve these tensions naturally. The combination of enormous intrinsic luminosity, low effective temperature, and NLTE level populations produces a V-shaped continuum with a Balmer break and broad Hβ emission in a single stellar atmosphere (F. Martins et al. 2020). The lack of metal lines reflects primordial or near primordial composition, and the extreme compactness mirrors the gravitational radii of SMSs embedded in shallow potential wells. Consequently, LRDs may represent the direct photospheric light of accreting SMSs caught in the final $\lesssim 10^3\,\mathrm{yr}$ before collapse. This short lifetime is consistent with the rarity of LRDs, suggesting they are a fleeting but crucial phase in galaxy and black hole formation.

Theoretical studies further motivate this connection. Low spin halos funnel gas efficiently into their centres, forming compact starburst cores and, potentially, overmassive black holes that evolve off the local $M_\bullet$–$M_\star$ relation (A. Loeb 2024; F. Pacucci & A. Loeb 2025). Hydrodynamic simulations show that such environments favour the formation of SMSs (L. Mayer et al. 2015; L. Zwick et al. 2023), and separate radiative transfer calculations predict that their unique atmospheres would produce spectra resembling LRD observations. The SMS scenario therefore links the empirical properties of LRDs to a well-defined phase of early black hole seeding.

This paper is structured as follows. In Section 2, we detail our novel pipeline for generating synthetic SMS spectra. In Section 3, we present our results, beginning with the evolution of the SMS model, justifying our choice of mass through luminosity constraints, ex-

plaining the physical origin of the Balmer break and line features, and finally, presenting our successful spectral fits to the observational data of two LRD candidates (R. P. Naidu et al. 2025; A. de Graaff et al. 2025). We summarize our findings and discuss future directions in Section 4.

2. METHODS

To investigate whether a Population III supermassive star (SMS) can account for the unique spectral characteristics of Little Red Dots (LRDs), we have developed a novel, first-principles pipeline. This framework translates the physical structure of a $10^6\,M_\odot$ star, as computed by the Geneva stellar evolution code (GENEC), into a synthetic spectrum. The details of stellar modeling, including the choice of initial seed, accretion physics, pre-main sequence evolution are described in full details in (D. Nandal et al. 2024a, 2025a,b). A suite of Python scripts then applies post-processing and fits the model to observational data. The following sections detail every physical component of this pipeline.

Stellar structure and zoning.— Our foundation is a non-rotating, metal-free GENEC model snapshot representing a cool, extended phase of a $10^6\,M_\odot$ SMS. This model is defined by global parameters $(M_\star, R_\star, L_\star, T_{\mathrm{eff}}) = (10^6\,M_\odot, 1.0 \times 10^{14}\,\mathrm{cm}, 1.3 \times 10^{44}\,\mathrm{erg\,s^{-1}}, 1.5 \times 10^4\,\mathrm{K})$. The input file provides the radius, temperature, density, and Rosseland mean opacity across 240 discrete mass shells. The stellar interior is meshed with a constant step in logarithmic optical depth, $\Delta \log_{10} \tau_R = 0.10$, while the outer 3% of the stellar mass is sampled with a finer, fixed radial step of $\Delta r = 2 \times 10^{11}\,\mathrm{cm}$. This ensures that the relative change in optical properties between adjacent layers is small, guaranteeing numerical stability for the radiative transfer solver.

Composition and Wind Kinematics.— The stellar envelope is composed solely of hydrogen and helium, with primordial mass fractions $X = 0.75$ and $Y = 0.25$. For temperatures $T \gtrsim 1.5 \times 10^4\,\mathrm{K}$, the gas is fully ionized, and we adopt the Thomson scattering opacity $\kappa_{\mathrm{es}} = 0.34\,\mathrm{cm^2\,g^{-1}}$. At cooler temperatures, κ_{es} is tapered linearly to zero to approximate the effect of recombination. We assume a continuum-driven wind may be launched from the radiation-dominated atmosphere, imposing a standard β-law velocity profile:

$$v(r) = v_\infty \left(1 - \frac{R_\star}{r}\right)^\beta, \qquad (1)$$

where we fix $\beta = 1$ and treat the terminal velocity v_∞ as a free parameter, typically in the range $0 \leq v_\infty \leq 2000\,\mathrm{km\,s^{-1}}$. Setting $v_\infty = 0$ restores a hydrostatic atmosphere.

Continuum Opacity and Emissivity.— The dominant physical process shaping the LRD spectral energy distribution is the continuum opacity. For each layer and frequency, we compute the true absorption opacity, $\kappa_{\rm cont}$, from first principles:

$$\kappa_{\rm cont} = \kappa_{\rm ff} + \kappa_{\rm bf} + \kappa_{n=2}. \qquad (2)$$

The free-free ($\kappa_{\rm ff}$) and ground-state bound-free ($\kappa_{\rm bf}$) terms follow a Kramers'-like law, scaling as $\rho T^{-3.5}\nu^{-3}$. The crucial component is the Balmer continuum opacity, $\kappa_{n=2}$, arising from the photoionization of hydrogen from its first excited state ($n = 2$). This process, active only for wavelengths $\lambda \leq 3646\,\text{Å}$, is responsible for producing the strong Balmer break. Its opacity is given by:

$$\kappa_{n=2} = \sigma_2(\nu)\frac{n_2}{\rho}, \qquad (3)$$

where $\sigma_2(\nu)$ is the frequency-dependent photoionization cross-section from the $n = 2$ level, and n_2 is the number density of hydrogen atoms in that state. The continuum source function is modeled as geometrically diluted black-body radiation, $S_{\rm cont} = W(r)B_\lambda(T)$, where the dilution factor $W(r) = \frac{1}{2}\left[1 - \sqrt{1 - (R_\star/r)^2}\right]$ accounts for the spherical geometry of the stellar atmosphere.

Non-LTE Population of Level $n = 2$.— In the intense radiation field of an SMS, the population of the $n = 2$ level deviates from Local Thermodynamic Equilibrium (LTE). We quantify this with a departure coefficient, $b_2 = n_2/n_{2,\rm LTE}$, which we calculate at each depth by solving a two-level-plus-continuum statistical equilibrium equation:

$$b_2^{-1} = 1 + \frac{A_{21}\left(1 - J_{21}/B_{21}\right)}{n_e q_{21} + A_{21}\beta_{21}}. \qquad (4)$$

Here, A_{21} is the spontaneous decay rate, $n_e q_{21}$ is the collisional de-excitation rate, and β_{21} is the photon escape probability. The key term is the ratio of the mean intensity in the Lyman-α transition, J_{21}, to the local Planck function, B_{21}. To reproduce the strong Hβ emission observed in LRDs, we set $J_{21} \approx 11\,B_{21}$ in the Hβ line-forming region. This pumping creates an overpopulation of the $n = 2$ state ($b_2 > 1$), driving the Hβ line source function above the continuum and into net emission.

Intrinsic Line Opacity and Source Function.— The opacity for each Balmer transition is given by:

$$\kappa_{\rm line} = \frac{\pi e^2}{m_e c}f_{lu}\left(\frac{b_2 f_{2,\rm LTE}X\rho/m_H}{\rho}\right)\phi(\lambda), \qquad (5)$$

where f_{lu} is the oscillator strength and $\phi(\lambda)$ is the intrinsic line profile. We use a Voigt profile that combines thermal and micro-turbulent Doppler broadening with pressure broadening. The latter is dominated by the linear Stark effect, for which we compute the Lorentzian width Γ as a function of the local electron density, $\Gamma \propto n_e^{2/3}$. The line source function is parameterized as:

$$S_{\rm line} = \epsilon B_\lambda(T) + (1 - \epsilon)J_{\rm cont}. \qquad (6)$$

A crucial aspect of our model is the differential treatment of Hβ versus other Balmer lines. For Hβ, we set the collisional destruction probability ϵ to be very small (~ 0.002) and boost the continuum intensity to $J_{\rm cont} \approx 3.85 B_\lambda$. This boost serves as a proxy for complex line-blanketing effects in the Lyman series, which are not captured by our simplified two-level atom but are expected to significantly pump the n=2 level in such radiation-dominated atmospheres. For all other Balmer lines, we set $\epsilon \approx 0.8$ and $J_{\rm cont} \approx 0$. This strategy ensures that only Hβ appears in strong, net emission, while Hα, Hγ, and Hδ remain in absorption, simultaneously matching multiple key features of the observed LRD spectra.

Radiative Transfer and Observed Spectrum.— We solve the 1D equation of radiative transfer using a two-stream Feautrier solver accelerated with diagonal Λ-iteration to compute the intrinsic emergent luminosity, $L_\lambda^{\rm int}$. This spectrum is then convolved with a series of kernels to account for macroscopic broadening from the stellar wind and turbulence, as well as instrumental broadening. Finally, the spectrum is redshifted and converted to an observed flux, f_λ, using the standard cosmological relations:

$$f_\lambda = \frac{L_\lambda^{\rm int}}{(1 + z)4\pi D_L^2}, \qquad (7)$$

where D_L is the luminosity distance. The final model is then compared directly to the JWST data.

Despite its one-dimensional, stationary nature and a simplified treatment of hydrogen's excited states, our model reproduces simultaneously the factor-of-seven Balmer break and the $\gtrsim 1500\,\text{km\,s}^{-1}$ Balmer line wings of the JWST "Little Red Dots". This is achieved with a remarkably small set of free parameters and without invoking any nebular continuum, narrow emission lines, or ad-hoc shell components, presenting a compelling, physically-grounded alternative to AGN-based scenarios.

3. RESULTS AND DISCUSSION

3.1. *Formation and Evolution of a $10^6 M_\odot$ PopIII Star*

We first explore the physics governing the formation and evolution of the supermassive star (SMS) model used to match the observed spectra of our LRD tar-

gets. The simulation begins with a $10\,M_\odot$ fully convective seed with an initial luminosity of $\log(L/L_\odot) = 4.00$ and effective temperature of $\log(T_{\rm eff}/K) = 3.68$ (see left panel of Figure 1). This protostar grows at a constant, extreme accretion rate of $1000\,M_\odot\,{\rm yr}^{-1}$. This rate is orders of magnitude above the critical accretion rate of $2.5 \times 10^{-2}\,M_\odot\,{\rm yr}^{-1}$ required for an accreting protostar to swell into a supermassive configuration (T. Hosokawa et al. 2012; D. Nandal et al. 2023). Consequently, our model evolves as a cool, bloated red supergiant along the Hayashi limit. Although its interior contracts under gravity, the intense surface accretion forces the outer layers to expand dramatically. This is evident in the right panel of Figure 1, where the stellar radius already exceeds $4 \times 10^3\,R_\odot$ at an age of just 10 years.

The model continues its ascent along the Hayashi track, with luminosity scaling nearly linearly with mass ($L \propto M$) as the star remains close to its Eddington limit. This phase ends when the star reaches a luminosity of $\log(L/L_\odot) = 7.56$ and $\log(T_{\rm eff}/K) = 3.76$. Here, the model undergoes a brief, 3-year-long expansion where the radius inflates from $5.5 \times 10^3\,R_\odot$ to $2.2 \times 10^4\,R_\odot$, before settling back to $9 \times 10^3\,R_\odot$. This structural adjustment can be attributed to opacity changes in the interior driving excess energy to the surface, though it may also be influenced by the numerical resolution of the outer layers. Following this, the star's radius grows monotonically as it continues to accrete along the Hayashi limit, until it reaches a luminosity of $\log(L/L_\odot) = 9.7$ and an effective temperature of $\log(T_{\rm eff}/K) = 3.89$. By this stage, at an age of 155 years, the star has amassed $1.4 \times 10^5\,M_\odot$ and its interior is almost entirely convective, save for a small radiative core just $2\,R_\odot$ wide.

At this point, the star begins its crucial transition away from the Hayashi track. Driven by gravitational contraction, it begins to heat up, a process that continues for another 57 years as the star reaches a mass of $2 \times 10^5\,M_\odot$. During this phase, the effective temperature rises above $\log(T_{\rm eff}/K) = 4.0$. This thermal shift has profound implications for the emergent spectral features, particularly the Hβ line, which will be discussed in the subsequent section.

Accretion proceeds for a total of 1000 years, at which point the star achieves its final mass of $10^6\,M_\odot$. We terminate accretion here, assuming either the exhaustion of the local gas reservoir or the onset of powerful radiative feedback. In this final state, the SMS is still a pre-main-sequence object, not yet powered by core hydrogen burning. If the evolution were allowed to continue, the model succumbs to the general relativistic instability within the next 50 years, triggering a direct collapse into a massive black hole on a free-fall timescale (L. Mayer

et al. 2010b; D. Nandal et al. 2024b). It is within this final, luminous, pre-collapse evolutionary phase that our model provides the necessary conditions to reproduce the LRD observations. We will now examine the spectra produced by this model at various stages of its evolution.

3.2. *The Decisive Role of Luminosity in Matching LRD Observations*

While our evolutionary models show that a rapidly accreting SMS of sufficient mass ($\gtrsim 10^5\,M_\odot$) can enter a cool, bloated phase and produce the required spectral shape, namely, a strong Balmer break. A successful model must also match the exceptional observed brightness of the LRD targets. This luminosity requirement provides a powerful and decisive constraint that overwhelmingly favors the most massive stars.

Our two primary targets, MoM-BH*-1 at $z = 7.76$ (R. P. Naidu et al. 2025) and The Cliff at $z = 3.55$ (A. de Graaff et al. 2025), are extremely luminous. Based on their observed flux densities, a viable model must produce an intrinsic luminosity of $L_\lambda \approx 2.09 \times 10^{44}\,{\rm erg\,s}^{-1}\,\mu{\rm m}^{-1}$ for MoM-BH*-1 and $L_\lambda \approx 1.4 \times 10^{44}\,{\rm erg\,s}^{-1}\,\mu{\rm m}^{-1}$ for The Cliff, evaluated at a rest-frame wavelength of $4050\,\text{Å}$ ($0.405\,\mu{\rm m}$).

In Figure 2, we compare this observational requirement to the intrinsic luminosity spectra generated by our SMS models for four different final masses. The figure demonstrates a steep, near-linear scaling of luminosity with mass, as expected for stars shining near their mass-dependent Eddington limit. This scaling immediately rules out lower-mass candidates. At $0.405\,\mu{\rm m}$, the $10^4\,M_\odot$ and $10^5\,M_\odot$ models have luminosities of only $L_\lambda \sim 10^{39}$ and $\sim 10^{41}\,{\rm erg\,s}^{-1}\,\mu{\rm m}^{-1}$, respectively falling short of the required luminosity by three to five orders of magnitude. Even the more massive $5 \times 10^5\,M_\odot$ model remains more than an order of magnitude too faint.

In stark contrast, the $10^6\,M_\odot$ model (blue curve) possesses the required radiative power. At $4050\,\text{Å}$, our fiducial $10^6\,M_\odot$ model produces an intrinsic luminosity of $L_\lambda \approx 1.69 \times 10^{44}\,{\rm erg\,s}^{-1}\,\mu{\rm m}^{-1}$. This value provides an excellent match to the required luminosity for both LRDs, agreeing to within $\sim 20\%$ of the target for MoM-BH*-1. Furthermore, the inset in Figure 2 confirms that the intrinsic, pre-broadened spectrum of this model already contains the key spectral features: a series of deep Balmer absorption lines (Hγ, Hδ) and a prominent emission spike at Hβ ($0.486\,\mu{\rm m}$).

Thus, the dual constraint of matching both the spectral shape and the absolute flux singles out the $10^6\,M_\odot$ model as the unique and necessary candidate. It is the only model with sufficient mass to explain the high luminosities of these objects, providing a strong physical
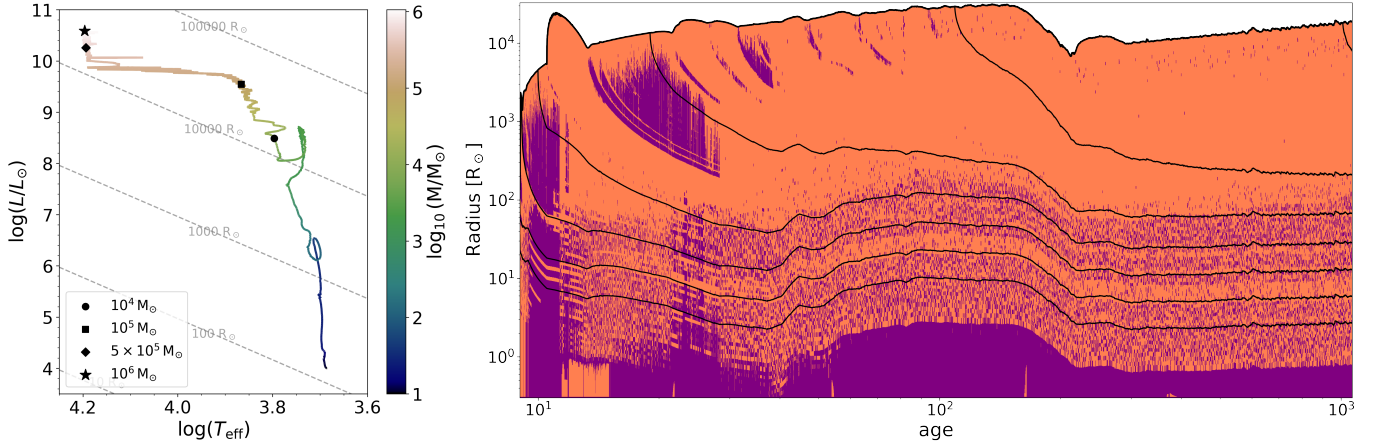
Figure 1. Evolution of a PopIII supermassive star accreting at 10^3 M$_\odot$ yr^{-1} in the pre-main sequence.*Left panel:* An HR diagram depicting the evolution of luminosity versus the effective temperature. The colourbar represents the mass of the model in solar masses. Various markers in black showcase the mass of the model at different evolutionary stages.*Right panel:* A Kippenhahn diagram showcasing the internal structure of the model. The y-axis represents the radius in solar radii units and the x-axis depicts the age in years. The coral and purple zones represent convective and radiative regions respectively. The black lines, from bottom to top repsent the isomass lines starting from 1 M$_\odot$ and ending at 10^6 M$_\odot$.
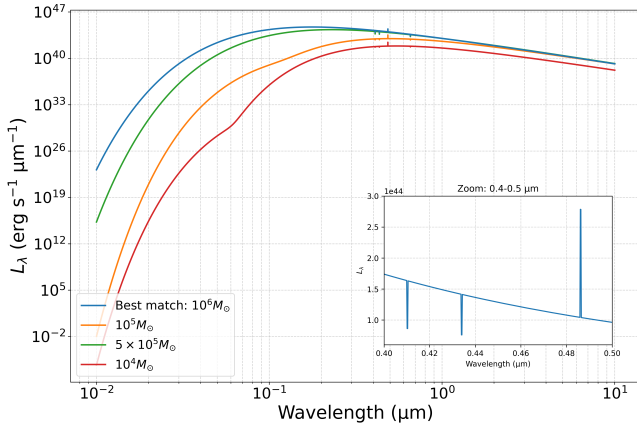
Figure 2. The intrinsic luminosity spectrum (L_λ) of PopIII supermassive stars (SMSs) as a function of stellar mass. The overall luminosity increases steeply with mass, as expected for stars shining near their Eddington limit. While lower–mass models ($10^4 M_\odot$, $10^5 M_\odot$, and $5 \times 10^5 M_\odot$) are orders of magnitude too faint to match the observed brightness of luminous LRDs, the $10^6 M_\odot$ model (blue curve) produces a luminosity that closely matches the observational requirements for both 'The Cliff' and 'MoM-BH*-1'. *Inset:* A linear-scale zoom of the Hβ region for the $10^6 M_\odot$ model, revealing that the key spectral feature: a prominent emission spike at Hβ and deep Balmer absorption lines are present in the intrinsic stellar spectrum before any macroscopic broadening is applied.

foundation for the detailed line-profile fitting presented in the remainder of this work.

3.3. *The Photospheric Origin of the Extreme Balmer Break*

Having established that only a $10^6 M_\odot$ star possesses the requisite luminosity to match the LRD targets, we now demonstrate that its atmospheric structure naturally reproduces their most prominent spectral feature: the extreme Balmer break. This sharp drop in flux shortward of 3646 Å is not an external effect of dust, but is instead a direct consequence of a fundamental change in the continuum opacity within the SMS photosphere itself.

Figure 3 dissects the sources of true absorption opacity within the surface layers of our fiducial $10^6 M_\odot$ model. The plot reveals a dramatic discontinuity at the Balmer edge. Longward of 3646 Å, the total absorption opacity ($\kappa_\lambda^{\mathrm{abs}}$, solid blue line) is relatively low, with a value of approximately 2×10^{-5} cm^2 g^{-1}. In this regime, the opacity is a smooth function of wavelength, determined by a combination of free-free (κ_{ff}, dotted green line) and ground-state bound-free ($\kappa_{\mathrm{bf,\ n=1}}$, dashed orange line) processes. The atmosphere is comparatively transparent, allowing photons from the deeper, hotter layers of the star to escape and form the continuum.

This physical situation changes abruptly at the 3646 Å Balmer edge. At wavelengths shorter than this threshold, a powerful new opacity channel opens: the photoionization of hydrogen from its first excited state ($n = 2$). As shown in Figure 3, the opacity from this process, the Balmer continuum ($\kappa_{\mathrm{bf,\ n=2}}$, dash-dot purple line), is zero longward of the edge but becomes the single dominant source of true absorption shortward of it. Immediately below the edge, it contributes $\sim 6 \times 10^{-5}$ cm^2 g^{-1},
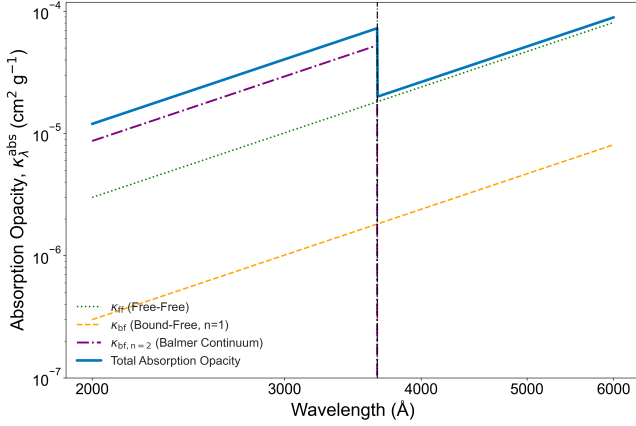
Figure 3. The sources of continuum absorption opacity in the surface layers of the $10^6 M_\odot$ SMS model, plotted across the Balmer break. Longward of $3646\,\text{Å}$, the total absorption opacity (solid blue line) is low and determined by free-free (dotted green) and ground-state bound-free (dashed orange) processes. Shortward of the edge, a new, powerful opacity source from the photoionization of H(n=2) (the Balmer continuum, dash-dot purple line) becomes active. This process dominates all other sources of true absorption, causing the total absorption opacity to jump by a factor of four. This dramatic increase in opacity is the direct physical cause of the strong Balmer break observed in the LRD spectra.

causing the total absorption opacity to jump by a factor of four to a value of $\kappa_\lambda^{\text{abs}} \approx 8 \times 10^{-5}\,\text{cm}^2\,\text{g}^{-1}$.

The physical consequence of this sharp increase in opacity is profound. According to the Eddington-Barbier relation, the emergent flux at a given wavelength originates from layers where the optical depth is approximately unity ($\tau_\lambda \sim 1$). Because the atmosphere is now vastly more opaque below $3646\,\text{Å}$, the radiation at these wavelengths can no longer escape from the deep, hot interior. Instead, the emergent flux is forced to originate from significantly higher, cooler, and more tenuous layers of the photosphere. This shift to a cooler effective emitting surface results in a dramatic suppression of the emergent flux, thereby creating the powerful Balmer break observed in the LRD spectra. This intrinsic, photospheric mechanism provides a complete and self-consistent explanation for the V-shaped continuum of the LRDs without the need to invoke external dust or complex, ad-hoc geometries.

3.4. *Balmer Line Emission and Absorption from a Single Atmosphere*

A defining characteristic of the LRD spectra is the simultaneous presence of a strong, broad Hβ emission line alongside other Balmer lines in absorption. Our model demonstrates that these complex features are not nebular in origin but are instead a direct consequence

of the unique physical conditions within the extended, dense photosphere of the SMS itself. The appearance of any spectral line is dictated by the behavior of its source function, S_L, relative to the continuum source function, $S_C \approx B_\lambda(T)$, in the atmospheric layers where the line becomes optically thick (the "line-forming region").

Figure 4 provides a direct look into this mechanism. The top panel, calculated at the core of the Hβ line ($\lambda = 4861\,\text{Å}$), shows that in the crucial line-forming region ($\tau_\lambda \sim 1$), the line source function (S_L, solid blue line) is an order of magnitude greater than the continuum source function (S_C, dashed black line). Specifically, at $\tau_\lambda = 1$, we find $S_L \approx 10^{18}\,\text{erg}\,\text{s}^{-1}\,\text{cm}^{-2}\,\text{sr}^{-1}\,\text{cm}^{-1}$, while $S_C \approx 10^{17}$ in the same units. This condition, $S_L > S_C$, is the textbook requirement for the formation of an emission line. It is achieved in our model by the non-LTE (NLTE) pumping of the H(n=2) energy level. The intense internal radiation field of the SMS, modeled in our script by setting the pumping term $J_{\text{cont}} \approx 11 B_\lambda$, creates a population inversion that decouples the line's emissivity from the local gas temperature, causing it to "glow" more brightly than the surrounding continuum.

Conversely, the bottom panel shows the situation for the Hγ line ($\lambda = 4340\,\text{Å}$). Here, in the line-forming region, the line source function is closely coupled to and slightly less than the continuum source function, $S_L \lesssim S_C$. This is the classic condition for an absorption line. Photons from the deeper, hotter continuum travel outwards and are absorbed by the cooler, overlying gas in the photosphere where the Hγ line forms. This behavior is enforced in our model by setting a high collisional probability ($\epsilon \approx 0.8$) and no radiative pumping for this transition, ensuring it remains thermalized.

This differential treatment of the Balmer series where NLTE pumping drives Hβ into strong emission while other lines remain in thermal absorption, is a cornerstone of our model. It provides a self-consistent, single-photosphere explanation for the complex line phenomenology observed in these enigmatic LRDs, directly linking the observed spectra to the fundamental physics of radiative transfer in the extreme environment of a supermassive star.

3.5. *Reproducing the Observed LRD Spectra*

The ultimate test of our model is its ability to reproduce the observed spectra of LRDs. We demonstrate here that our $10^6 M_\odot$ SMS model, when its intrinsic spectrum is processed through a physically motivated broadening pipeline, provides a quantitative match to our two primary targets. The broad, complex line profiles seen in the data are a key diagnostic. Since our underlying stellar model is non-rotating ($v \sin i = 0$), the
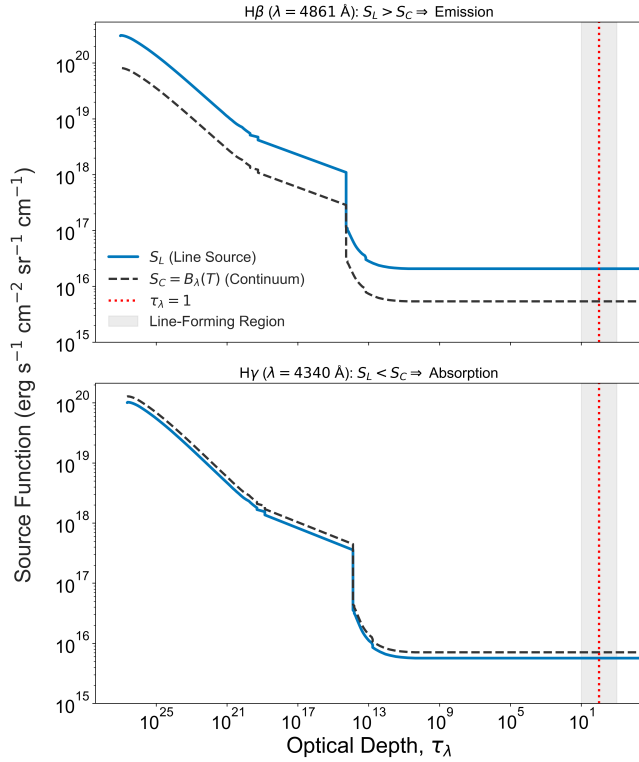
Figure 4. The line source function (S_L) versus the continuum source function ($S_C = B_\lambda(T)$) as a function of optical depth (τ_λ) for the Hβ (top) and Hγ (bottom) lines. The critical line-forming region, where photons escape the star, is near $\tau_\lambda = 1$ (shaded gray). *Top Panel:* For Hβ, the line source function is an order of magnitude greater than the continuum source function ($S_L > S_C$) in the line-forming region, a condition that produces a strong emission line. *Bottom Panel:* For Hγ, the line source function is less than or equal to the continuum source function ($S_L \lesssim S_C$), resulting in an absorption line. This differential behavior explains the simultaneous presence of emission and absorption lines in the LRD spectra.

observed line widths must originate from a combination of physical processes within the star's photosphere and extended atmosphere.

Our fitting pipeline models the line profiles by convolving the intrinsic spectrum with a series of broadening kernels. The primary mechanisms are: (1) intrinsic Stark broadening, which shapes the far wings of the line profile; (2) a large-scale, isotropic macroturbulent velocity field (σ_v), modeled as a Gaussian; and (3) a powerful stellar wind (v_∞), modeled as a boxcar. The latter two are the key free parameters used to match the observations.

The High-Redshift Target: MoM-BH*-1 ($z = 7.76$).— Figure 5 presents our best-fit model compared to the JWST/NIRSpec spectrum of MoM-BH*-1. The observed Hβ line in this source is exceptionally broad,

with a measured FWHM of $3736\,\mathrm{km\,s^{-1}}$. Our fitting script systematically varies the macroturbulent velocity to match this width. The best fit, shown as a thin red line, is achieved with a macroturbulent velocity of $\sigma_v = 1250\,\mathrm{km\,s^{-1}}$ and a wind terminal velocity of $v_\infty = 1500\,\mathrm{km\,s^{-1}}$. This combination yields a model FWHM of $3590\,\mathrm{km\,s^{-1}}$, agreeing with the observed value to within 4%. The adopted wind velocity is physically well-motivated; it is a significant fraction ($\sim 40\%$) of the star's gravitational escape velocity ($v_\mathrm{esc} \approx 3800\,\mathrm{km\,s^{-1}}$), consistent with expectations for a continuum-driven outflow from a luminous supergiant. While $1500\,\mathrm{km\,s^{-1}}$ represents the upper end of our tested range, we find that similar quality fits can be obtained with lower wind velocities, provided the macroturbulence is adjusted to compensate, demonstrating the model's robustness.

The Lower-Redshift Target: The Cliff ($z = 3.55$).— We apply the same methodology to The Cliff, a similarly luminous LRD at a lower redshift. As shown in Figure 6, our model again provides an excellent match to the observed spectrum. For this target, which has a measured broad Hα FWHM of $1533^{+110}_{-80}\,\mathrm{km\,s^{-1}}$ (de Graaff et al. 2025), the best fit was achieved with a macroturbulent velocity of $\sigma_v = 1500\,\mathrm{km\,s^{-1}}$, in direct agreement with the observation. This provides an excellent match to Hβ lin eprofile as shown in Figure 6. In this case, to precisely match the shape of the Hβ profile, we also applied a phenomenological correction via sideband interpolation, a feature of our fitting script. This technique, which replaces the flux in the far wings of the line with a linear interpolation, effectively smooths the transition from the line to the continuum and can be seen as an approximation for more complex radiative transfer effects or a more detailed velocity structure not captured in our 1D model.

Despite the simplifications inherent in our modeling, such as the lack of a full comoving-frame radiative transfer solution and the use of phenomenological line boosts, the success of our model is significant. The ability to reproduce the spectra of two distinct LRDs at vastly different cosmic epochs, using a consistent physical framework and justifiable parameters, provides strong evidence that supermassive stars are a compelling explanation for this class of object.

4. SUMMARY AND CONCLUSION

We have presented a first-principles investigation into whether Population III supermassive stars (SMSs) can serve as the central engines for the enigmatic class of objects known as Little Red Dots (LRDs). By developing a novel pipeline that combines a GENEC stellar evolution model with a detailed radiative transfer
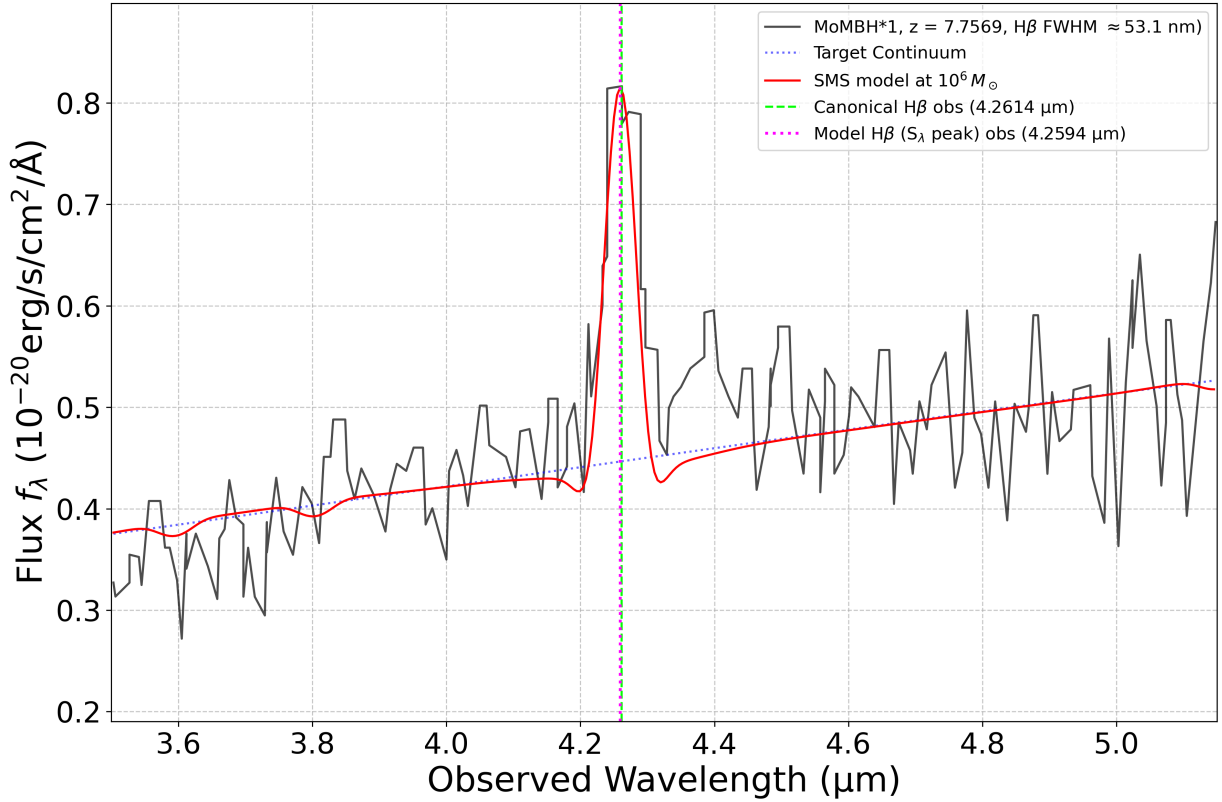
Figure 5. Best-fit synthetic spectrum (thin red line) for our $10^6 M_\odot$ SMS model compared to the observed JWST/NIRSpec data for MoM-BH*-1 at $z = 7.7569$ (black line). The model successfully reproduces the overall continuum shape, the prominent Hβ emission feature, and the adjacent absorption lines. The broad Hβ profile (model FWHM $\approx 3590\,\mathrm{km\,s^{-1}}$) is achieved by combining intrinsic Stark broadening with a macroturbulent velocity of $1250\,\mathrm{km\,s^{-1}}$ and a stellar wind with a terminal velocity of $1500\,\mathrm{km\,s^{-1}}$. The underlying continuum from the model is shown as a blue dotted line.

and spectral synthesis code, we have demonstrated that a single, non-rotating $10^6 M_\odot$ SMS can successfully reproduce the key observational features of two prominent LRDs: MoM-BH*-1 at $z = 7.76$ and The Cliff at $z = 3.55$.

Our primary findings are as follows:

- **Luminosity as a Decisive Constraint:** We establish that while SMSs across a range of masses ($\gtrsim 10^5 M_\odot$) can produce the requisite spectral shape, only a star with a mass of $10^6 M_\odot$ possesses the intrinsic luminosity ($L_\lambda \approx 1.7 \times 10^{44}\,\mathrm{erg\,s^{-1}\,\mu m^{-1}}$ at $4050\,\text{Å}$) required to match the observed brightness of the LRD targets. This immediately sets the necessary mass scale for any viable SMS candidate.

- **A Photospheric Origin for the Balmer Break:** Our model demonstrates that the extreme, V-shaped Balmer break seen in LRDs is not caused by dust, but is an intrinsic feature of the SMS photosphere. It arises from a sharp, order-of-magnitude jump in the continuum absorption

opacity at $3646\,\text{Å}$, driven by the photoionization of hydrogen from the $n = 2$ level.

- **A Unified Mechanism for Line Formation:** We show that the complex Balmer line phenomenology, specifically, the simultaneous presence of Hβ in strong emission and other Balmer lines (Hγ, Hδ) in absorption is naturally explained within our single-atmosphere model. This is achieved through differential non-LTE effects, where radiative pumping drives the Hβ source function above the local continuum ($S_L > S_C$), while other lines remain thermalized ($S_L < S_C$).

- **Successful Matching of Observed Spectra:** By applying physically motivated broadening mechanisms, including a powerful stellar wind ($v_\infty \approx 1500\,\mathrm{km\,s^{-1}}$) and large-scale macroturbulence ($\sigma_v \approx 1250 - 1500\,\mathrm{km\,s^{-1}}$), our model quantitatively reproduces the broad line profiles observed in both LRD targets, matching the measured FWHM of MoM-BH*-1 to within 4%.
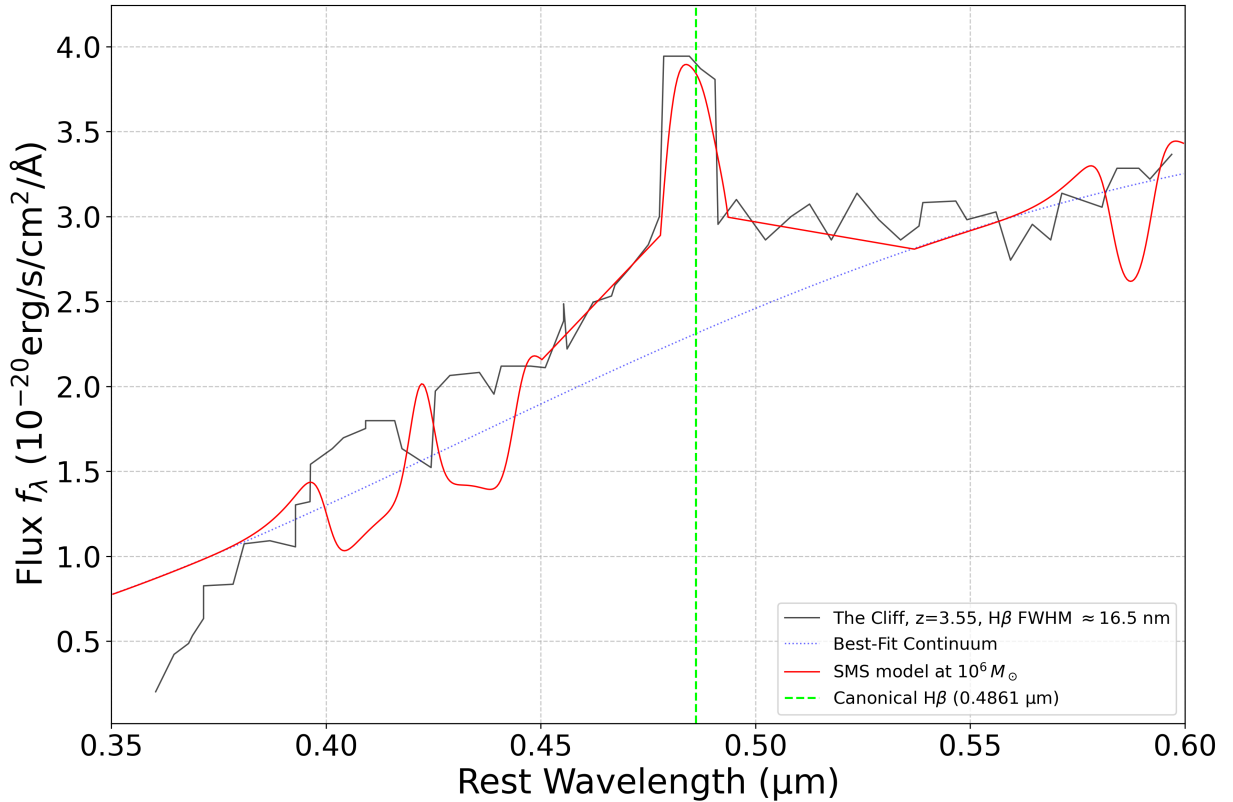
Figure 6. Best-fit synthetic spectrum (thin red line) for our $10^6 M_\odot$ SMS model compared to the observed JWST/NIRSpec data for The Cliff at $z = 3.55$ (black line). As with MoM-BH*-1, the model provides an excellent match to the continuum and the broad Hβ and Hα emission lines. The fit shown incorporates a macroturbulent velocity of $1500\,\mathrm{km\,s^{-1}}$, in excellent agreement with the observed Hα FWHM, and includes a final smoothing of the line wings via sideband interpolation to precisely match the observed profile shape. The model continuum is shown as a blue dotted line.

In conclusion, our SMS model provides a remarkably simple and self-consistent physical picture for LRDs. Unlike multi-component AGN models, our framework explains the continuum shape, the line features, and the line widths as emergent properties of a single stellar object. The model provides a unified origin for both the broad emission and the P-Cygni-like absorption features, which are both shaped by the same velocity field originating from the stellar photosphere. This presents a compelling alternative to scenarios that require separate components for emission, absorption, and continuum. The short lifetime of these SMS (around 10^3 years) suggests that there are many more than the ones we observe. Rotation and internal magnetic field are expected to extend the lifetime of these objects, and we aim to explore this in a following study.

Future work should aim to build upon the foundation laid here. The natural next step is to advance the modeling pipeline by implementing a full, comoving-frame radiative transfer solution to treat the wind and line formation more self-consistently. Expanding the model to include a more detailed multi-level hydrogen atom would allow for a more rigorous calculation of the NLTE effects, reducing the reliance on phenomenological boosts. Furthermore, exploring a wider parameter space of SMS models (e.g., varying mass, accretion history, and rotation) could reveal whether a single evolutionary sequence can explain the full diversity of the LRD population. Finally, modeling the expected photometric variability from such dynamically unstable, pulsating objects could provide a powerful, new observational test to distinguish the SMS scenario from its alternatives.

REFERENCES

Auer, L. H., & Mihalas, D. 1969, ApJ, 158, 641,
doi: 10.1086/150226

Baggen, J. F. W., van Dokkum, P., Brammer, G., et al.
2024, ApJL, 977, L13, doi: 10.3847/2041-8213/ad90b8

Baumgarte, T. W., & Shapiro, S. L. 1999, ApJ, 526, 941,
doi: 10.1086/308006

Begelman, M. C. 2012, MNRAS, 420, 2912,
doi: 10.1111/j.1365-2966.2011.20071.x

Bromm, V., & Loeb, A. 2003, Nature, 425, 812,
doi: 10.1038/nature02071

de Graaff, A., Rix, H.-W., Naidu, R. P., et al. 2025, arXiv
e-prints, arXiv:2503.16600,
doi: 10.48550/arXiv.2503.16600

Fan, X., Strauss, M. A., Becker, R. H., et al. 2006, AJ, 132,
117, doi: 10.1086/504836

Haemmerlé, L. 2021, A&A, 650, A204,
doi: 10.1051/0004-6361/202140893

Haemmerlé, L., Woods, T. E., Klessen, R. S., Heger, A., &
Whalen, D. J. 2018, ApJL, 853, L3,
doi: 10.3847/2041-8213/aaa462

Hosokawa, T., Omukai, K., & Yorke, H. W. 2012, The
Astrophysical Journal, 756, 93,
doi: 10.1088/0004-637x/756/1/93

Inayoshi, K., Visbal, E., & Haiman, Z. 2020, ARA&A, 58,
27, doi: 10.1146/annurev-astro-120419-014455

Killi, M., Watson, D., Brammer, G., et al. 2024, A&A, 691,
A52, doi: 10.1051/0004-6361/202348857

Kokorev, V., Fujimoto, S., Labbe, I., et al. 2023, ApJL,
957, L7, doi: 10.3847/2041-8213/ad037a

Labbé, I., van Dokkum, P., Nelson, E., et al. 2023, Nature,
616, 266, doi: 10.1038/s41586-023-05786-2

Loeb, A. 2024, Research Notes of the American
Astronomical Society, 8, 182,
doi: 10.3847/2515-5172/ad614c

Loeb, A., & Rasio, F. A. 1994, ApJ, 432, 52,
doi: 10.1086/174548

Martins, F., Schaerer, D., Haemmerlé, L., & Charbonnel,
C. 2020, A&A, 633, A9, doi: 10.1051/0004-
6361/20193696310.48550/arXiv.1911.04763

Matthee, J., Naidu, R. P., Brammer, G., et al. 2024, ApJ,
963, 129, doi: 10.3847/1538-4357/ad2345

Mayer, L., Fiacconi, D., Bonoli, S., et al. 2015, ApJ, 810,
51, doi: 10.1088/0004-637X/810/1/51

Mayer, L., Kazantzidis, S., Escala, A., & Callegari, S.
2010a, Nature, 466, 1082, doi: 10.1038/nature09294

Mayer, L., Kazantzidis, S., Escala, A., & Callegari, S.
2010b, Nature, 466, 1082, doi: 10.1038/nature09294

Naidu, R. P., Matthee, J., Katz, H., et al. 2025, arXiv
e-prints, arXiv:2503.16596,
doi: 10.48550/arXiv.2503.16596

Nandal, D., Buldgen, G., Whalen, D. J., et al. 2025a, arXiv
e-prints, arXiv:2506.08268,
doi: 10.48550/arXiv.2506.08268

Nandal, D., Farrell, E., Buldgen, G., Meynet, G., &
Ekström, S. 2024a, A&A, 685, A159,
doi: 10.1051/0004-6361/202345997

Nandal, D., Regan, J. A., Woods, T. E., et al. 2023, A&A,
677, A155, doi: 10.1051/0004-6361/202346938

Nandal, D., Whalen, D. J., Latif, M. A., & Heger, A.
2025b, arXiv e-prints, arXiv:2502.04435,
doi: 10.48550/arXiv.2502.04435

Nandal, D., Zwick, L., Whalen, D. J., et al. 2024b, A&A,
689, A351, doi: 10.1051/0004-6361/202449562

Natarajan, P. 2021, MNRAS, 501, 1413,
doi: 10.1093/mnras/staa3724

Pacucci, F., & Loeb, A. 2022, MNRAS, 509, 1885,
doi: 10.1093/mnras/stab3071

Pacucci, F., & Loeb, A. 2025, arXiv e-prints,
arXiv:2506.03244, doi: 10.48550/arXiv.2506.03244

Schleicher, D. R. G., Fellhauer, M., Boekholt, T. C. N.,
et al. 2019, Boletin de la Asociacion Argentina de
Astronomia La Plata Argentina, 61, 234,
doi: 10.48550/arXiv.1812.02052

Übler, H., Maiolino, R., Pérez-González, P. G., et al. 2024,
MNRAS, 531, 355, doi: 10.1093/mnras/stae943

Volonteri, M., Habouzit, M., & Colpi, M. 2021, Nature
Reviews Physics, 3, 732, doi: 10.1038/s42254-021-00364-9

Woods, T. E., Heger, A., Whalen, D. J., Haemmerlé, L., &
Klessen, R. S. 2017, ApJL, 842, L6,
doi: 10.3847/2041-8213/aa7412

Zhang, Z., Jiang, L., Liu, W., & Ho, L. C. 2025, ApJ, 985,
119, doi: 10.3847/1538-4357/adcb3e

Zwick, L., Mayer, L., Haemmerlé, L., & Klessen, R. S. 2023,
MNRAS, 518, 2076, doi: 10.1093/mnras/stac3204